

Traveling Wave-Based Fault Location Algorithm for Hybrid Multi-Terminal Circuits

R. J. Hamidi, *Graduate Student Member, IEEE* and H. Livani, *Member, IEEE*

Abstract—This paper presents a traveling wave-based fault location algorithm for hybrid multi-terminal transmission systems that consist of one onshore overhead line and multiple offshore submarine cables. Such hybrid transmission systems are common for interconnection of offshore wind farms to the main grid. The input to the algorithm is synchronized transient voltage measurements from all the receiving ends. These measurements are obtained by optical voltage transducers equipped with global positioning system (GPS) receivers for time synchronization. The discrete wavelet transformation (DWT) is utilized to decompose the mode-1 voltages at the receiving ends. The first wave arrival times are then obtained by observing the squares of wavelet transformation coefficient (WTC²s). The transient simulations and the post-fault analysis are carried out using EMTP-RV and MATLAB Wavelet Toolbox, respectively. The accuracy, limitations, and capabilities of the proposed algorithm are presented and discussed for different fault conditions.

Index Terms—Fault location, hybrid transmission systems, submarine cables, traveling waves, wavelet transformation.

I. INTRODUCTION

NOWADAYS, a growing number of wind farms are deployed in offshore areas. Offshore wind farms are often connected to the main grid via a hybrid transmission system consisting of an overhead line, a collector bus, and several submarine (subsea) cables, as shown in Fig. 1 [1], [2]. Accurate fault location is a necessary post-fault tool that results in a quick system restoration after a fault and prevents more economic losses. Fault location in submarine transmission systems is a challenging task due to the following reasons:

- Wind farms are mostly built in wild seas, which are harsh working places for maintenance crews.
- Submarine cables are usually Cross-linked PolyEthylene (XLPE) insulated [1]-[3]. The fault arc does not solidly burn through the entire XLPE insulation [4]. Therefore, the fault path is available only when the cable is energized, and thus, offline fault location methods have limited practical applicability.
- Hybrid transmission systems have a relatively complex structure that makes fault location a difficult task.

This paper is based upon work partially supported by Department of Electrical and Biomedical Engineering, University of Nevada, Reno.

Reza Jalilzadeh Hamidi and H. Livani are with Department of Electrical and Biomedical Engineering, University of Nevada, Reno (emails: reza.j.hamidi@gmail.com, hlivani@ieee.org).

Historically, fault location methods are mainly divided into three categories [5]: power frequency-based (i.e., impedance-based), traveling wave-based, and artificial intelligence-based methods. In [6] and [7], it is shown that the zero-sequence impedance of a fault loop and the fault location are not linearly proportional for cross-bonded cables because of discontinuities at the cross-bondings. References [8] and [9] show that the impedance-based methods estimate the fault location in cross-bonded cables only when the faulty major section is identified. In [10], a fault location method based on distributed sequential impedances is presented. This method identifies the faulty section in cross-bonded cables for only single-line-to-ground (SLG) faults. In [11], a power frequency-based fault location method is presented that locates SLG faults in underground cables without laterals. In [12], a power frequency-based method is improved using characteristic frequencies corresponding to every possible fault location. Due to the above-mentioned limitations, power frequency-based fault location methods have limited applicability for cables.

Traveling wave-based fault location methods are more accurate and reliable compared to power frequency-based methods [13]. The advent of optical high-voltage transducers together with high-frequency transient recorders (TRs) makes traveling wave-based methods practical [14]. In [15], fault initiated traveling waves are extracted and used for fault location. The use of discrete wavelet transformation (DWT) for extracting the traveling waves from the modal voltages is first proposed in [16]. Reference [17] presents a traveling wave-based fault location method for three-terminal transmission systems consisting of three overhead lines. In [18], a fault location method based on current traveling waves for multi-terminal transmission systems is proposed. In [19], synchronized arrival times of the traveling waves are utilized for faulty line identification and fault location in overhead transmission grids. References [2] and [7] demonstrate that the modal transformation reduces the cross-bonding effect, and the use of traveling wave-based fault location methods are thus applicable to hybrid transmission systems. In [20], a single-ended traveling wave-based fault location method for hybrid transmission systems consisting of an overhead line and an underground cable is presented. In [21], a support vector machine (SVM) classifier is utilized for faulty segment and faulty half identification. This method is applicable on the systems comprising one overhead line and one underground cable. In [22], an online fault location

method for underground cables is presented that uses sheath currents. In [23], a traveling wave-based fault location method is presented for a hybrid three-terminal transmission system with one overhead line and two submarine cables. Hybrid multi-terminal transmission systems are widely used for interconnection of offshore wind farms to the main grid. However, custom-designed fault location methods for the mentioned systems have been less addressed in the literature and still remain an open problem.

In this paper, the preliminary results in [23] are extended and a traveling wave-based fault location method for hybrid multi-terminal transmission systems consisting of one overhead line and multiple submarine cables is presented. The sensitivity of the proposed algorithm is evaluated for the following parameters: fault type, grounding system, fault inception angle (FIA), transducer bandwidth, TR sampling frequency, fault resistance, non-ideal fault, and non-linear arc. The advantages of the proposed method are: 1) It is not severely affected by the fault parameters. 2) The proposed method is based on an analytical solution and does not require a large number of simulations for training data as required by artificial intelligence-based methods. 3) It estimates fault location via the weighted least squares (WLS) method, which uses the first arrival times of fault induced traveling waves. Therefore, the fault location errors due to measurement uncertainties are reduced.

Our proposed fault location algorithm has the following major steps: 1) Synchronized transient voltages of power system terminals are measured through optical transducers equipped with GPS signal receivers. 2) The Clarke's transformation is applied to the measured voltages for obtaining the mode-1 voltages. 3) Discrete wavelet transformation (DWT) is applied to the calculated mode-1 voltages, and the first arrival times are measured by observing the squares of wavelet transformation coefficient (WTC²s). 4) The faulty segment identification and fault location are executed using the differences among the measured first arrival times.

The remainder of this paper is organized as follows: in Section II, the proposed fault location method is provided. In Section III, an illustrative test case, the sensitivity assessment, and comparison are provided. The conclusion is stated in Section IV.

II. PROPOSED FAULT LOCATION METHOD

The proposed fault location method is based on the following assumptions and requirements: 1) Optical voltage transducers are available at all power system terminals [16], [18]. 2) The terminals are equipped with GPS signal receivers for synchronizing the transient voltage measurements [18]. 3) Measuring devices at the joint point (so-called, collector bus, "J" in Fig. 1) are not required. 4) The wave traveling time (i.e., the time that a traveling wave passes along a segment) in each segment is known a priori [2], [16], [17].

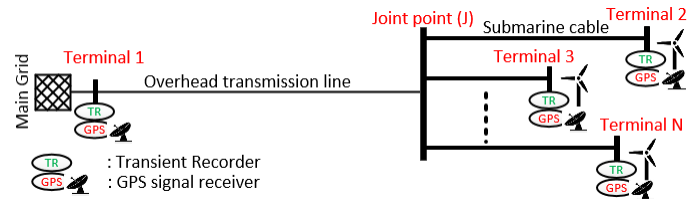


Fig. 1. One-line diagram of hybrid multi-terminal transmission systems (equipped with transient recorders and GPS signal receivers).

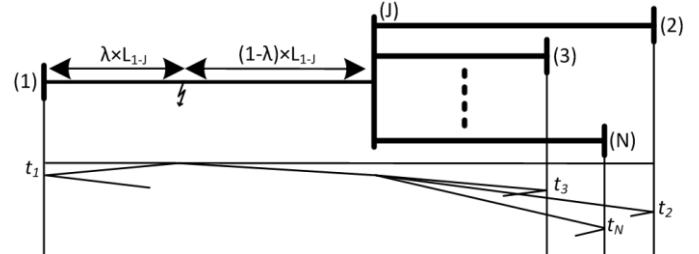


Fig. 2. Lattice diagram of traveling waves initiated by a fault in Segment 1-J.

A. Theory of the Proposed Method

Synchronized transient voltage measurements are obtained using TRs equipped with GPS signal receivers. DWT is applied to the calculated mode-1 voltages, and the first wave arrival times are measured by observing the WTC²s. Then, the arrival time differences are compared to the a priori known wave traveling time differences. This provides sufficient information for identifying the faulty segment. Once the faulty segment is identified, the fault location is estimated.

Fig. 2 shows the lattice diagram of a fault in the overhead line (i.e., Segment 1-J). The fault induced first arrival times at Terminals 1 to N are

$$\begin{bmatrix} \tilde{t}_1 \\ \tilde{t}_2 \\ \vdots \\ \tilde{t}_N \end{bmatrix} = \begin{bmatrix} \lambda & 0 & \dots & 0 \\ (1-\lambda) & 1 & \dots & 0 \\ \vdots & \vdots & \ddots & \vdots \\ (1-\lambda) & 0 & \dots & 1 \end{bmatrix} \begin{bmatrix} \tau_1 \\ \tau_2 \\ \vdots \\ \tau_N \end{bmatrix} + \begin{bmatrix} t_f \\ t_f \\ \vdots \\ t_f \end{bmatrix} + \begin{bmatrix} \varepsilon_1 \\ \varepsilon_2 \\ \vdots \\ \varepsilon_N \end{bmatrix} \quad (1)$$

where \tilde{t}_1 to \tilde{t}_N [s] are the measured first arrival times at Terminals 1 to N due to an unknown fault location on Segment 1-J. λ is the unknown ratio of the fault-to-terminal distance to the faulty segment length as shown in Fig. 2. τ_1 to τ_N [s] are the known wave traveling times in Segments 1-J to N-J, t_f [s] represents fault inception time, which is also unknown, and $\varepsilon_i \sim \mathcal{N}(0, \sigma_i^2)$, $\forall i = 1, 2, \dots, N$ are zero-mean Gaussian noises with σ_i^2 variances. The noises are independent, but non-identical. t_f in (1), can be canceled out by subtraction of any two arrival times. Therefore, \tilde{t}_{mn} is defined as

$$\tilde{t}_{mn} = \tilde{t}_m - \tilde{t}_n, \forall (m, n) = 1, 2, \dots, N \quad (2)$$

where \tilde{t}_m and \tilde{t}_n [s] are the measured first arrival times, m and n are terminal indices. Applying (2) to (1) yields

$$\Delta \tilde{\mathbf{t}} = \begin{bmatrix} 0 & \tilde{t}_{12} & \dots & \tilde{t}_{1N} \\ \tilde{t}_{21} & 0 & \dots & \tilde{t}_{2N} \\ \vdots & \vdots & \ddots & \vdots \\ \tilde{t}_{N1} & \tilde{t}_{N2} & \dots & 0 \end{bmatrix} \quad (3)$$

where $\Delta \tilde{\mathbf{t}}$ is the matrix form of arrival time differences. Each

$\tilde{\tau}_{mn}$ can have only one of the following general forms

$$\begin{cases} \tilde{\tau}_{mn} = (2\lambda - 1)\tau_m - \tau_n + \varepsilon_{mn}, & \text{if } m\text{-}J \text{ is faulty} \\ \tilde{\tau}_{mn} = (1 - 2\lambda)\tau_n + \tau_m + \varepsilon_{mn}, & \text{if } n\text{-}J \text{ is faulty} \\ \tilde{\tau}_{mn} = \tau_m - \tau_n + \varepsilon_{mn}, & \text{neither } m\text{-}J \text{ nor } n\text{-}J \text{ is faulty} \end{cases} \quad (4)$$

In the upper and lower triangular parts of the matrix $\Delta\tilde{\boldsymbol{\tau}}$, there are $(N - 1)$ elements related to the faulty segment and the remaining elements are related to the non-faulty segments.

The differences between each pair of the wave traveling times are shown with $\Delta\boldsymbol{\tau}$ as

$$\Delta\boldsymbol{\tau} = \begin{bmatrix} 0 & \tau_{12} & \dots & \tau_{1N} \\ \tau_{21} & 0 & \dots & \tau_{2N} \\ \vdots & \vdots & \ddots & \vdots \\ \tau_{N1} & \tau_{N2} & \dots & 0 \end{bmatrix} \quad (5)$$

where $\tau_{mn} = \tau_m - \tau_n$, and the wave traveling times are known a priori. In order to compare $\Delta\tilde{\boldsymbol{\tau}}$ with $\Delta\boldsymbol{\tau}$, the matrix $\boldsymbol{\Delta}$ is defined as follows

$$\boldsymbol{\Delta} = |\Delta\tilde{\boldsymbol{\tau}} - \Delta\boldsymbol{\tau}| \quad (6)$$

where $|\cdot|$ denotes the absolute value. $\boldsymbol{\Delta}$ is a symmetrical matrix with zero diagonal elements. Referring to (4) and (5), the differences between each $\tilde{\tau}_{mn}$ and its corresponding τ_{mn} related to non-faulty segments are relatively small (i.e., they are not exactly zero due to the measurement uncertainties). Therefore, a Δ_{mn} related to a non-faulty segment is relatively small. On the contrary, the difference between each $\tilde{\tau}_{mn}$ and its corresponding τ_{mn} related to the faulty segment is large, and therefore, the corresponding Δ_{mn} is large. Thus, the largest values in $\boldsymbol{\Delta}$ have an index (m or n) equal to the faulty segment, and they are also located in one row and its corresponding column. Accordingly, the row/column number with $(N - 1)$ maximal values indicates the faulty segment.

In order to identify the faulty segment, the matrix $\boldsymbol{\Delta}$ is first calculated. Then, the $(N - 1)$ maximal values in $\boldsymbol{\Delta}$ are identified. If they are located in the same row/column, the row/column number (denoted by c^*) identifies the ending terminal of the faulty segment (i.e., all the segments have a common end ‘‘J’’, therefore, with one terminal index, the faulty segment can be identified), and thus, the Segment $c^*\text{-}J$ is faulty. Otherwise, the faulty segment is unidentifiable and the proposed method is not able to find the fault location. The ability of the proposed method in detection of the faulty segment is discussed in Appendix A.

Once the faulty segment is identified, the elements on the $c^*\text{-th}$ column of $\Delta\tilde{\boldsymbol{\tau}}$ are utilized to provide $(N - 1)$ equations for estimation of λ as follows

$$\tilde{\tau}_{mc^*} = (1 - 2\lambda)\tau_{c^*} + \tau_m + \varepsilon_{mc^*}, \forall m = 1, 2, \dots, N, m \neq c^* \quad (7)$$

where c^* is the terminal index corresponding to the identified faulty segment ($c^*\text{-}J$). τ_{c^*} refers to the wave traveling time in the identified faulty segment. τ_m denotes the wave traveling time in non-faulty segments. Equation (7) is written in matrix form as

$$\Delta\tilde{\boldsymbol{\tau}}_{(N-1) \times 1}^* = -2\boldsymbol{\tau}_{(N-1) \times 1}^* \lambda + \boldsymbol{\tau}_{(N-1) \times 1}^* + \boldsymbol{\varepsilon}_{(N-1) \times 1} \quad (8)$$

where

$$\Delta\tilde{\boldsymbol{\tau}}^* = [\tilde{\tau}_{1c^*}, \tilde{\tau}_{2c^*}, \dots, \tilde{\tau}_{mc^*}]^T, \forall m = 1, 2, \dots, N, m \neq c^*$$

$$\boldsymbol{\tau}^* = [\tau_{c^*}, \tau_{c^*}, \dots, \tau_{c^*}]^T$$

$$\boldsymbol{\tau} = [\tau_1, \tau_2, \dots, \tau_m], \forall m = 1, 2, \dots, N, m \neq c^*$$

$$\boldsymbol{\varepsilon} = [\varepsilon_1 - \varepsilon_{c^*}, \varepsilon_2 - \varepsilon_{c^*}, \dots, \varepsilon_m - \varepsilon_{c^*}]^T, \forall m = 1, 2, \dots, N, m \neq c^*.$$

In order to make (8) more readable, $\boldsymbol{b} = \boldsymbol{\tau}^* + \boldsymbol{\tau} - \Delta\tilde{\boldsymbol{\tau}}^*$ is defined, and (8) is rewritten as

$$2\boldsymbol{\tau}_{(N-1) \times 1}^* \lambda = \boldsymbol{b}_{(N-1) \times 1} + \boldsymbol{\varepsilon}_{(N-1) \times 1} \quad (9)$$

Equation (9) is an overdetermined set of linear equations, therefore, λ is estimated using the WLS method as

$$\min_{\lambda} (2\boldsymbol{\tau}^* \lambda - \boldsymbol{b})^T \boldsymbol{R}^{-1} (2\boldsymbol{\tau}^* \lambda - \boldsymbol{b}) \quad (10)$$

Additional explanations for the WLS-based method are provided in Appendix B. Once $\hat{\lambda}$ is calculated (i.e., the estimated value of λ) the fault location is calculated by

$$EFD = \hat{\lambda} \times L \quad (11)$$

where EFD [mi] is the estimated fault-to-terminal distance and L is the length of the identified faulty segment [mi].

B. Algorithm

Fig. 3 shows the flowchart of the proposed algorithm with the following steps:

1. Transient three-phase voltages at all terminals are synchronously measured through optical voltage transducers equipped with GPS signal receivers.
2. The Clarke's transformation is applied to the measured voltages to obtain mode-1 voltages. The usage of mode-1 voltages reduces the effect of environmental parameters [7].
3. DWT is utilized to calculate wavelet transformation coefficients (WTCs). We use Daubechies-4 (db-4) mother wavelet in scale-1 for time-frequency decomposition of the synchronized mode-1 voltages at all terminals. A typical fault induced distortion in the voltage waveform, db-4 mother wavelet, and the resulted normalized WTC² are provided in Appendix C.
4. The first wave arrival times ($\tilde{\tau}$) at all the terminals are obtained by observing the WTC².
5. Time differences between each pair of the synchronized arrival times ($\tilde{\tau}_{mn}$) are calculated using (2).
6. In order to compare the matrix $\Delta\tilde{\boldsymbol{\tau}}$ with $\Delta\boldsymbol{\tau}$, the matrix $\boldsymbol{\Delta}$ is calculated using (6).
7. $(N - 1)$ maximal values in the matrix $\boldsymbol{\Delta}$ are found.
8. If all the maximal values are in the same row/column, the row/column number is denoted by c^* , and the faulty segment is $c^*\text{-}J$. Otherwise, the faulty segment is unidentifiable and the proposed method fails to find the fault location.

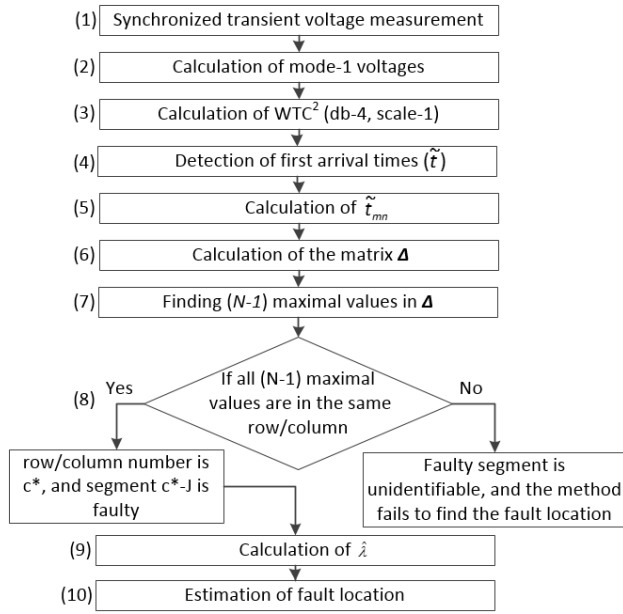


Fig. 3. The flowchart of the proposed fault location algorithm.

9. Having found the faulty segment, one can find $\hat{\lambda}$ using (10).
10. The fault location is estimated using (11).

In the following section, the simulation results and the related discussions are presented.

III. SIMULATION RESULTS AND DISCUSSIONS

In order to evaluate the proposed fault location algorithm, we used EMTP-RV and MATLAB Wavelet Toolbox to carry out the transient simulations and post-fault analysis, respectively. The test case is a 170-kV, 60-Hz, hybrid seven-terminal transmission system. The transmission system consists of one overhead line and six submarine cables, as shown in Fig. 4. The frequency-dependent line and cable models (EMTP FD and FDQ models) are used for the overhead transmission line and cables. The lengths of the segments and traveling times are provided in Table I. The sheaths of the cables are assumed to be fully cross-bonded and steel wire armour is continuously grounded [23]. Overhead line specifications are based on [24]. Two different cable types are used for submarine cables (i.e., Cable type 1 and 2 are based on Nexans, “TKRA 170 kV” and “A2XS(FL)2Y RM 87/150 170 kV”, respectively [25]). Cable type 1 is used for Segments 2-J, 3-J, and 4-J, and cable type 2 is used for the Segments 5-J, 6-J, and 7-J. Transmission line transposition increases its attenuation constant [26]. Therefore, the traveling waves initiated by faults are more mitigated, and fault location becomes more challenging. Accordingly, we used a fully transposed overhead line in our simulation studies. In order to consider the effect of measurement uncertainties, zero-mean Gaussian noises with variances of $(V_p \times 0.01)$ are added to all transient voltage measurements, and V_p is the peak voltage of the system voltage [21]. Referring to Fig. 1, the main grid and wind farms are simulated using voltage sources behind series impedances with the following resistance and inductance

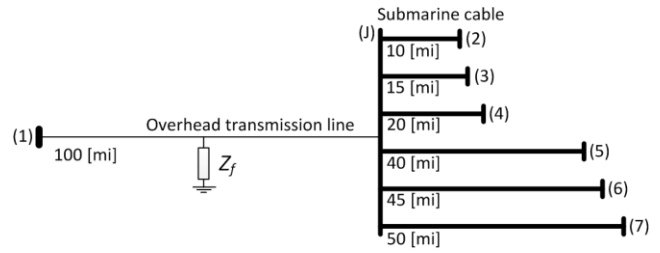


Fig. 4. One-line diagram of the test case (seven-terminal hybrid system).

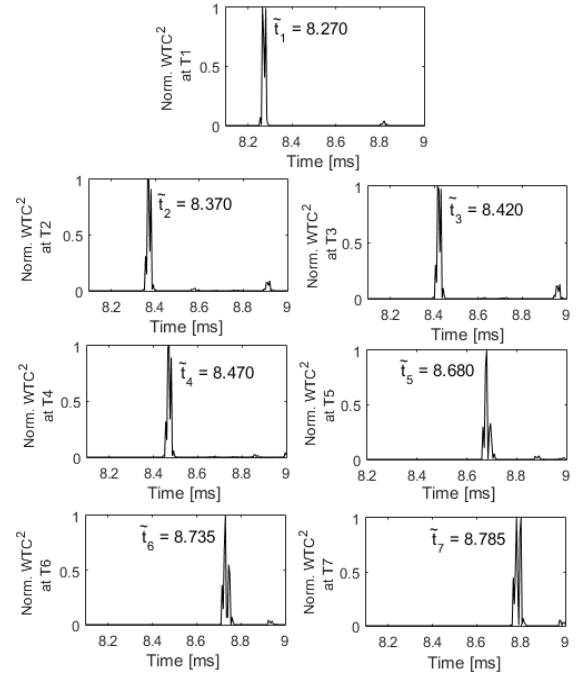


Fig. 5. WTC²s of mode-1 voltages in scale-1, SLG fault in the overhead line at 50 mi from Terminal 1, $F_s = 200$ kHz, and $Z_f = 1 \Omega$.

matrices:

$$R_m = \begin{bmatrix} 1.8 & 0.4 & 0.4 \\ 0.4 & 1.8 & 0.4 \\ 0.4 & 0.4 & 1.8 \end{bmatrix}, L_m = \begin{bmatrix} 0.0132 & 0.0053 & 0.0053 \\ 0.0053 & 0.0132 & 0.0053 \\ 0.0053 & 0.0053 & 0.0132 \end{bmatrix}$$

$$R_w = \begin{bmatrix} 2.5 & 0.8 & 0.8 \\ 0.8 & 2.5 & 0.8 \\ 0.8 & 0.8 & 2.5 \end{bmatrix}, L_w = \begin{bmatrix} 0.0185 & 0.0074 & 0.0074 \\ 0.0074 & 0.0185 & 0.0074 \\ 0.0074 & 0.0074 & 0.0185 \end{bmatrix}$$

where R_m [Ω] and L_m [H] are related to the main grid, R_w [Ω] and L_w [H] are related to the wind farms.

A. Illustrative Test Case

The steps of the proposed method for an SLG fault are provided in this section. The SLG fault is located in the middle of the overhead line (Segment 1-J) with the following conditions: $Z_f = 1 \Omega$, which is the fault impedance, $FIA = 8^\circ$, and $F_s = 200$ kHz, which is the sampling frequency of the TRs. Fig. 5 shows the normalized WTC²s and the corresponding first arrival times based on steps 1 to 5, described in “Section II-B”. Table I provides wave traveling time differences ($\Delta\tau$) and the measured arrival time differences ($\Delta\tilde{t}$). The matrix Δ is also provided in Table I, and the six maximal values are located in the first row/column. Hence, $c^* = 1$, and therefore, Segment 1-J is identified as the faulty segment. According to (8) to (10), the below vectors are used to find the fault location in the identified faulty segment,

TABLE I. TRAVELING TIMES IN DIFFERENT SEGMENTS

Segment Lengths [mi] ¹	$L_{1-J}=100,$ $L_{2-J}=10, L_{3-J}=15, L_{4-J}=20,$ $L_{5-J}=40, L_{6-J}=45, L_{7-J}=50$
Wave Traveling Times (τ) [μ s] at 75 kHz ²	$\tau_{1-J} = 550,$ $\tau_{2-J} = 105, \tau_{3-J} = 155, \tau_{4-J} = 205,$ $\tau_{5-J} = 410, \tau_{6-J} = 460, \tau_{7-J} = 510$
$\Delta\tau =$	$\begin{bmatrix} 0 & 445 & 395 & 345 & 140 & 90 & 40 \\ -445 & 0 & -50 & -100 & -305 & -355 & -405 \\ -395 & 50 & 0 & -50 & -255 & -305 & -355 \\ -345 & 100 & 50 & 0 & -205 & -255 & -305 \\ -140 & 305 & 255 & 205 & 0 & -50 & -100 \\ -90 & 355 & 305 & 255 & 50 & 0 & -50 \\ -40 & 405 & 355 & 305 & 100 & 50 & 0 \end{bmatrix}$
$\Delta\tilde{\tau} =$	$\begin{bmatrix} 0 & -100 & -150 & -200 & -410 & -465 & -515 \\ 100 & 0 & -50 & -100 & -310 & -365 & -415 \\ 150 & 50 & 0 & -50 & -260 & -315 & -365 \\ 200 & 100 & 50 & 0 & -210 & -265 & -315 \\ 410 & 310 & 260 & 210 & 0 & -55 & -105 \\ 465 & 365 & 315 & 265 & 55 & 0 & -50 \\ 515 & 415 & 365 & 315 & 105 & 50 & 0 \end{bmatrix}$
$\Delta =$	$\begin{bmatrix} 0 & 545 & 545 & 545 & 550 & 555 & 555 \\ 545 & 0 & 0 & 0 & 5 & 10 & 10 \\ 545 & 0 & 0 & 0 & 5 & 10 & 10 \\ 545 & 0 & 0 & 0 & 5 & 10 & 10 \\ 550 & 5 & 5 & 5 & 0 & 5 & 5 \\ 555 & 10 & 10 & 10 & 5 & 0 & 0 \\ 555 & 10 & 10 & 10 & 5 & 0 & 0 \end{bmatrix}$

¹ L denotes segment length.

² As sampling frequency is 200 kHz, the measurement frequency contents are up to 100 kHz, and in wavelet scale-1, the frequency range from 50 to 100 kHz is considered. Therefore, wave traveling times at 75 kHz are utilized.

$$\begin{aligned} \Delta\tilde{\tau}^* &= [100,150,200,410,465,515]^T, \\ \tau^* &= [550,550,550,550,550,550]^T, \\ \tau &= [105,155,205,410,460,510]^T, \text{ and} \\ \mathbf{b} &= [555,555,555,550,545,545]^T. \end{aligned}$$

The system voltage is 170 kV and noise variances in all the measurements are $170000 \times \sqrt{2/3} \times 0.01$, therefore, $\mathbf{R} = \text{diag}(2800,2800,2800,2800,2800,2800)$ based on Appendix B. The estimated λ is $\hat{\lambda} = 0.50075$ and the fault location is calculated using (11) as $EFD = 0.50075 \times 100 = 50.075$ mi. The fault location errors are finally calculated using

$$err = \frac{|AFD - EFD|}{L} \times 100\% \quad (12)$$

where err is the fault location error, AFD [mi] is the actual fault distance, EFD [mi] is the estimated fault distance, and L is the faulty segment length [mi]. The error related to the illustrative case is $\frac{|50-50.075|}{100} \times 100 = 0.075\%$.

B. Sensitivity Assessment

In this section, the sensitivity of the proposed algorithm is evaluated for the following parameters: fault type, grounding system, FIA, optical transducer bandwidth, TR sampling frequency, fault resistance, non-ideal fault, and non-linear arc.

1) Fault Type and Grounding

In this paper, all five types of fault (i.e., single-line-to-ground (SLG), line-to-line (LL), line-to-line-to-ground (LLG),

TABLE II. RELATION BETWEEN FAULT TYPE AND ERROR

Faulty Seg.	AFD [mi]	Fault Type				
		SLG	LL	LLG	3L	3LG
1-J	1	0.174	0.174	0.173	0.173	0.173
	50	0.080	0.080	0.080	0.079	0.080
	99	0.296	0.294	0.295	0.295	0.294
2-J	1	3.010	3.010	3.012	2.998	2.998
	5	0.375	0.374	0.374	0.372	0.372
	9	8.174	8.174	8.175	8.167	8.167
3-J	1	3.454	3.455	3.454	3.454	3.454
	7	0.146	0.146	0.146	0.143	0.144
	14	7.059	7.048	7.091	7.052	7.051
4-J	1	2.687	2.692	2.698	2.688	2.689
	10	0.198	0.198	0.201	0.198	0.198
	19	5.375	5.374	5.376	5.366	5.366
5-J	1	0.268	0.268	0.267	0.266	0.266
	20	0.013	0.012	0.012	0.011	0.011
	39	0.467	0.467	0.468	0.468	0.466
6-J	1	0.335	0.334	0.334	0.332	0.332
	22	0.012	0.012	0.012	0.011	0.011
	44	0.499	0.504	0.505	0.488	0.487
7-J	1	0.272	0.273	0.273	0.272	0.272
	25	0.017	0.015	0.016	0.014	0.014
	49	0.406	0.404	0.407	0.405	0.404

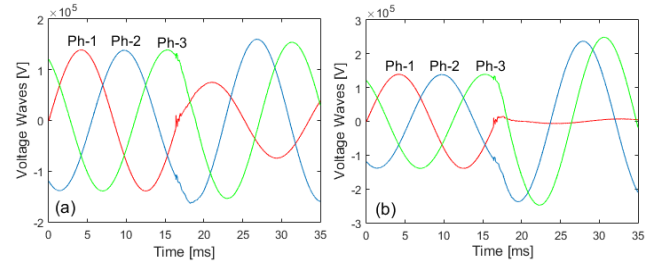


Fig. 6. Three phase voltages at Terminal 2 (SLG fault in the middle of Segment 2-J, $Z_f = 1 \Omega$, $FIA = 8^\circ$). (a) Grounded system. (b) Ungrounded system.

three-phase (3L), and three-phase-to-ground (3LG)) are studied. The magnitudes of the traveling waves increase for multiple-phase type of faults. Therefore, the signal-to-noise ratio (SNR) increases, and the fault initiated traveling waves are more detectable. Table II provides the average of the fault location errors for 1000 Monte Carlo simulations (MCSs) ($Z_f = 1 \Omega$, $FIA = 8^\circ$, $F_s = 200$ kHz) at different locations. In each MCS, Gaussian random numbers are added to the simulated transient voltages to account for the measurement noises. As it is observed in Table II, the proposed method is not affected by the fault type since the traveling waves initiated by SLG faults are large enough to be detected.

The effect of grounding system is also studied in this paper. Although the fault currents are smaller in ungrounded systems compared to that in grounded systems, the voltages are more distorted in ungrounded systems, as shown in Fig. 6 (SLG fault in the middle of Segment 2-J, $Z_f = 1 \Omega$, and $FIA = 8^\circ$). Therefore, the traveling wave magnitudes are larger and more detectable. As the proposed method is less efficient in grounded systems, the studies are limited to grounded systems.

2) Fault Inception Angle (FIA)

FIA affects the severity of the traveling waves initiated by a

TABLE III. EFFECT OF FIA

Faulty Segment	AFD [mi]	FIA [$^{\circ}$]			
		5	6	7	8
1-J	1	N/A	N/A	✓	✓
	99	N/A	N/A	N/A	✓
2-J	1	N/A	✓	✓	✓
	9	N/A	✓	✓	✓
3-J	1	N/A	✓	✓	✓
	14	N/A	✓	✓	✓
4-J	1	N/A	✓	✓	✓
	19	N/A	N/A	✓	✓
5-J	1	N/A	✓	✓	✓
	39	N/A	N/A	✓	✓
6-J	1	N/A	N/A	✓	✓
	44	N/A	N/A	✓	✓
7-J	1	N/A	N/A	✓	✓
	49	N/A	N/A	N/A	✓

N/A shows that the proposed method is not applicable.

✓ shows that the proposed method is applicable.

TABLE IV. RELATION BETWEEN THE SAMPLING FREQUENCY AND ERRORS

Faulty Seg.	AFD [mi]	F_s [kHz]	Error [%]	Faulty Seg.	AFD [mi]	F_s [kHz]	Error [%]
1-J	50	100	0.74	5-J	20	100	1.03
		200	0.08			200	0.01
2-J	5	100	2.38	6-J	22	100	0.95
		200	0.37			200	0.01
3-J	7	100	0.43	7-J	25	100	0.73
		200	0.14			200	0.01
4-J	10	100	2.44				
		200	0.19				

fault. As the FIA of a fault decreases, SNRs of the arriving waves decrease. Thus, detection of the traveling waves, and estimation of the fault location become more challenging. This concept is shown in Appendix C. Table III shows the effect of FIA on the proposed method. As the closest locations to the terminals and joint point are the most challenging locations for the proposed method, SLG faults with different FIAs at those places are studied and the results are given in Table III. The location of the faults with the minimum FIA of 8° are estimated by the proposed method ($Z_f = 1 \Omega$, $F_s = 200$ kHz). However, the location of the faults with smaller FIAs can be estimated for segments with lesser attenuation factors (i.e., attenuation factor equals $e^{-\alpha l}$, where α is attenuation constant, l is segment length [mi], [27]) or in less noisy situations.

3) Measuring Device Characteristics

An optical voltage transducer has a limited bandwidth. According to the Nyquist-Shannon's sampling theorem, frequency contents up to half of the sampling frequency of TRs can be measured. Hence, transducers together with TRs filter out high frequency contents of the transient voltages, and thus, the sharpness and magnitudes of the measured arriving waves reduce. Consequently, they become less detectable by DWT. Furthermore, as sampling frequency decreases, the proposed method resolution decreases [28]. Table IV shows the relation between the sampling frequency and the proposed

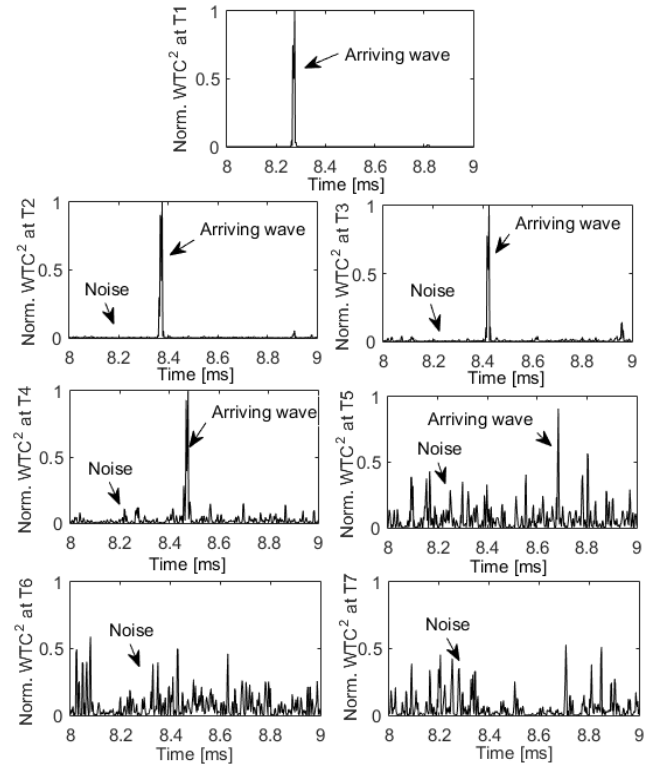


Fig. 7. Noise and arriving waves for a fault in the middle of Segment 1-J ($F_s = 500$ kHz, $Z_f = 1 \Omega$, $FIA=8^{\circ}$). The arriving waves at Terminals 1 to 4 are distinguishable from noise. However, the arriving waves at Terminals 5 to 7 disappears in the noise because of the larger attenuation factors of Segments 5-J, 6-J and 7-J.

algorithm accuracy for SLG faults at the given locations ($Z_f = 1 \Omega$, $FIA = 8^{\circ}$). It is noted that the accuracy of the proposed method increases as sampling frequency increases. On the other hand, the attenuation constants of the line and cables increase for higher frequencies of traveling waves. Therefore, the higher frequencies of traveling waves mitigate more and the traveling waves received at the terminals fade in the noise.

Fig. 7 shows normalized WTC^2 s related to the arriving waves induced by a fault identical to that in the illustrative test case. However, the sampling frequency is 500 kHz. It is observed that the arriving waves are well-distinguishable from the noise in Segment 1-J whose attenuation factor is 0.6274 at 187.5 kHz (for 50 mi, $\alpha = 0.009323$). Cable type 1 is used for Segments 2-J, 3-J, and 4-J and their attenuation factors are: 0.4365, 0.2885, and 0.1906 at 187.5 kHz, respectively ($\alpha = 0.082897$). Therefore, the arriving waves are still distinguishable from the noise as shown in Fig. 7. Cable type 2 is used for Segments 5-J, 6-J, and 7-J and their attenuation factors are: 2.8833×10^{-4} , 1.0403×10^{-4} , and 3.7537×10^{-5} at 187.5 kHz ($\alpha = 0.203785$), respectively. Therefore, arriving waves mitigate more, and consequently, the traveling waves disappear in the noise. Thus, the attenuation factors limit the highest applicable sampling frequency. However, higher sampling frequencies can be utilized in a less noisy situation, with higher DWT scales such as scale-2, or using the suggestions in [29] and [30] for reducing the noise effects.

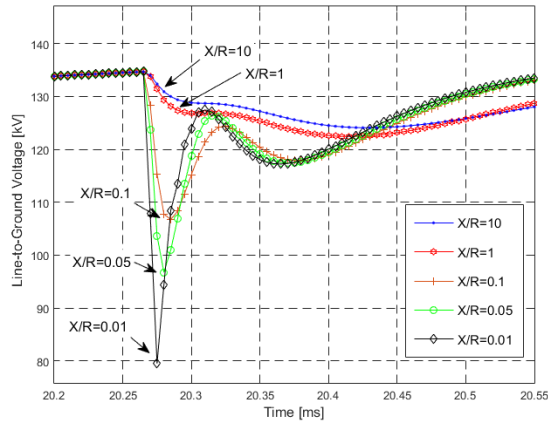


Fig. 8. The mode-1 voltages at the overhead line terminal for faults in the middle of the overhead line, $Z_f = R + jX_L = 10 \Omega$ and X/R ratio is variant.

4) Fault Resistance

The proposed method is evaluated for a range of fault resistances. As the fault resistance increases, the magnitudes of the fault initiated traveling waves decrease. Therefore, the traveling waves are prone to vanish because of attenuation factors and noises. The proposed method is able to estimate the location of a fault with a resistance up to 150Ω ($FIA = 8^\circ$, and $F_S = 200$ kHz).

5) Non-Ideal Faults

In this section, the effect of fault impedance (Z_f in Fig. 4) on the proposed method performance is studied. As a common practice, a resistive Z_f is considered in the literature. However, when a fault occurs between phases and ground wires or towers, the inductive part of Z_f becomes larger [31], [32]. Fig. 8 shows the effect of inductive fault impedances on traveling wave shapes. Total fault impedance is constant in all the cases, however, the X/R ratio varies ($Z_f = R + jX_L = 10 \Omega$). The fault impedances with larger X/R ratios generate traveling waves with smooth shapes. Consequently, the detectability of traveling waves degrades. Our simulation studies indicate that faults with $X/R \leq 71$, which corresponds to $L/R \leq 0.19$ H/ Ω , and $FIA \geq 8^\circ$ enable traveling waves to be detectable using DWT with db-4 mother wavelets and $F_S = 200$ kHz. As stated in [31] and [32], the inductive part of a fault impedance is usually small compared to its resistance. Hence, the proposed method is not affected by usual inductive faults in power systems. As for R-C fault impedances, the capacitive part does not make the traveling wave smooth. Therefore, R-C faults do not affect the proposed method performance.

6) Non-Linear Arc

The proposed algorithm is evaluated for long non-linear arcs that can occur in the overhead segment. A long arc is a non-linear fault influenced by a number of factors (e.g., the convection of the air and plasma, wind speed, pressure, and humidity) [33]. An arc in the air has two main stages:

- The first stage is the arc leader propagation in which the air gap breaks down and provides an ionized hot plasma channel [33] and [34]. The arc leader propagation for string insulator or rod-plane is modeled as [33]

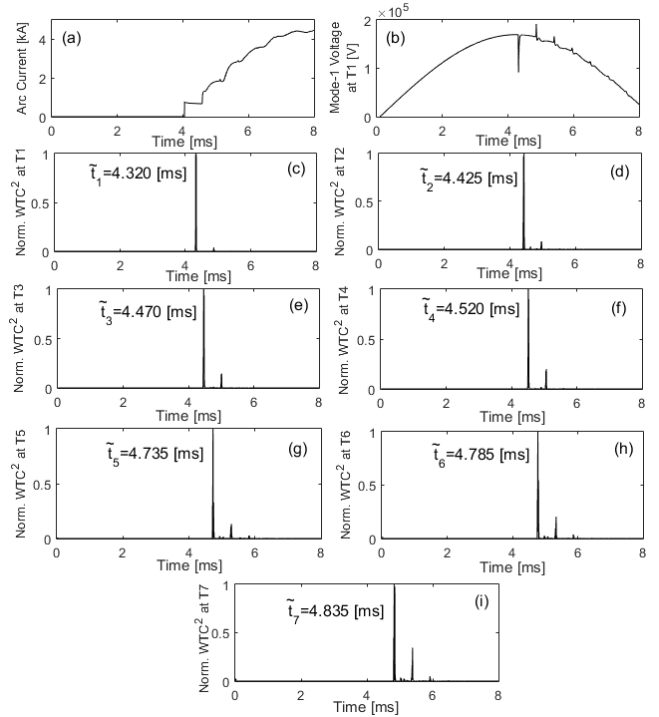


Fig. 9. The effects of arc leader propagation and long arc on the proposed method (fault in the overhead line at 50 mi from Terminal 1, $F_S = 200$ kHz). (a) The current through arc channel. (b) The mode-1 voltage at Terminal 1. (c)-(i) Normalized WTC^2 s at Terminals 1 to 7.

$$\begin{cases} v = k_1 \frac{V^2}{(D-x)} + k_2 \frac{Vi}{(D-x)} \left(\frac{x}{D}\right) \\ i = C_1 \cdot V \cdot v \end{cases} \quad (13)$$

where v is the arc leader propagation velocity [m/s], V [V] is the voltage across the air gap, i is the pre-discharge current [A], D and x [m] are the gap and leader lengths, respectively, and $C_1 = 5 \times 10^{-10}$ F/m according to [33]. We assume D is 0.3 m. The following parameters are utilized for simulations mostly based on [35]: $V = V_p \sin(2\pi \times 60 \times t)$, $V_p = 138.8$ kV that equals to 170 kV (LL-RMS), $k_1 = 2 \times 10^{-7}$ and $k_2 = 3 \times 10^{-3}$ for both positive and negative leaders.

- The second stage considers the dynamic behavior of an established long arc in which the arc resistance is non-linear and time-variant. Long arcs are modeled as [36]

$$\begin{cases} R_{arc} = 1/g \\ dg/dt = 1/\tau (G - g) \\ G = |i_{arc}|/V_{st} \end{cases} \quad (14)$$

where R_{arc} [Ω] is the time-varying arc resistance, g [S] is the time-varying arc conductance, i_{arc} [kA] is the arc current, G [S] is the stationary arc conductance, τ [s] is the arc time constant, and V_{st} [kV] is the stationary arc voltage, defined as

$$V_{st} = (u_0 + r \cdot |i_{arc}|) \times l \quad (15)$$

where u_0 [V/cm] is the constant voltage per arc length, r [m Ω /cm] is the arc resistance per length, and l [cm] is the arc length. The following parameters are utilized for the simulation study: $\tau = 10^{-3}$ s, $u_0 = 12$ V/cm, $r = 2$ m Ω /cm, and $l = 40$ cm.

Similar to the illustrative test case, the arc fault is located at

50 mi from Terminal 1 and $F_S = 200$ kHz. The fault current through the arc is shown in Fig. 9(a) to demonstrate the arc leader behavior. As it is observed, there is a sharp increase in the arc current during the first stage that generates large and sharp traveling waves. Fig. 9(b) shows the mode-1 voltage at Terminal 1 in which a sharp change in the voltage waveform is observed due to the fault induced traveling waves. Fig. 9(c)-(i) show the resulting WTC²s and their corresponding arrival times. The estimated fault location error is 0.08%. Thus, considering the second row of Table II, the proposed method accuracy does not deviate for non-linear arcs since they generate sharp large-amplitude traveling waves.

C. Error Assessment

One thousand MCSs for SLG faults ($Z_f = 1 \Omega$, $FIA = 8^\circ$, and $F_S = 200$ kHz) at every mile along the segments are carried out. A small portion of the faults are not correctly identified due to the measurement uncertainties. The unsuccessful fault locations in the case studies are as follows:

a) For faults at 99, 98, 97, and 96 mi from Terminal 1, the faulty segment is not correctly identified in 78, 58, 29, 8% of MCSs, respectively. b) For the faults at 44 mi from Terminal 6, 9% of the faults are not correctly identified. c) For the faults at 49 and 48 mi from Terminal 7, 16 and 8% of the faults are not correctly identified. For the other locations, the faults are identified in all Monte Carlo case studies.

Fig. 10 shows the average of the fault location errors in the logarithmic plane for all segments. A common trend is observed in all the segments, that is, the fault location errors decrease for the faults in the middle of the segments. Additionally, the faults close to the terminals and joint point lead to higher fault location errors. Furthermore, the faults close to the joint point result in higher errors compared to the faults near the terminals in accordance with [18], [20], and [21]. The fault location errors in the cables are larger compared to the errors in the overhead line since (12) is used for calculation of the errors and the shorter lengths of the cables lead to larger errors. The average errors related to the Segments 2-J, 3-J, and 4-J are larger compared to the errors in the literature because the lengths of these segments are shorter than the lengths in the literature [18]-[21] and [37].

D. Cable Aging

The inductance of a cable increases with cable aging. Therefore, traveling wave velocity decreases, and consequently, wave traveling time increases [38]. As the proposed method is based on a priori known wave traveling times, its accuracy degrades with cable aging. This shortcoming can be addressed by introducing a correction factor, which translates the changes in cable parameters to a change in traveling wave velocity. The correction factor can be determined by carrying out site tests in certain time intervals or by employing a parameter estimation tool.

E. Comparison

The accuracy and requirements of the proposed method are compared with the existing methods in the literature. The average errors are calculated and presented in Table V for

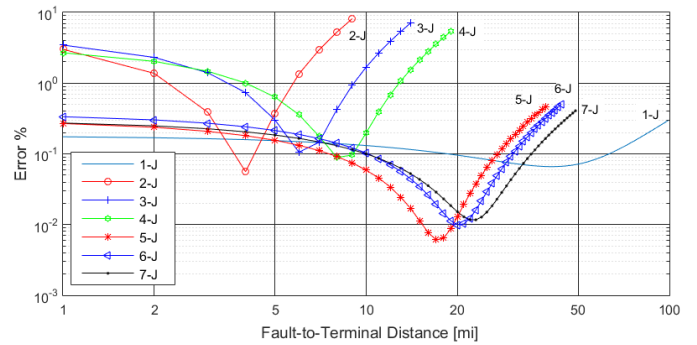


Fig. 10. Fault location errors along the segments, $Z_f = 1 \Omega$, $FIA = 8^\circ$, $F_S = 200$ kHz.

TABLE V. COMPARISON OF THE FAULT LOCATION METHODS

System Topology	S/A ¹	P/T ²	Error Ave. [%]	Noise	Number of Meas.	Ref.
UC ³	-	P	2.74	No	1	[10]
1-Segment	-	P	1.73	No	1	[11]
UC	-	T	1.132	Yes	1	[39]
1-Segment	-	T	0.43	No	3	[40]
UC	S	T	0.81	Yes	1	[21]
2-Segment	-	T	0.3	Real ⁴	2	[41]
Hybrid	S	T	1.37	No	3	[23]
2-Segment	S	T	0.36	Yes	7	Proposed Method
Hybrid	S	T				
3-Terminal						
Hybrid						
7-Terminal						

¹ S/A indicates synchronous or asynchronous measurements.

² P/T indicates power frequency-based or traveling wave-based fault location methods.

³ UC indicates underground cable.

⁴ Only one real experience is reported.

providing an insight into the accuracy of other methods. As it is observed from Table V, traveling wave-based fault location methods are more accurate compared to power frequency-based (i.e., impedance-based) methods. It is also observed that the proposed method has less error compared to the existing methods, however, it requires synchronized transient recorders at all terminals which can be economically justified for important transmission systems such as offshore wind power interconnection.

IV. CONCLUSION

This paper proposes a traveling wave-based fault location algorithm for hybrid multi-terminal transmission systems consisting of one overhead line and multiple submarine cables. Hybrid transmission systems are common for interconnection of offshore wind farms to the main grid. The proposed algorithm uses synchronized transient voltage measurements at all ending terminals. The measurements are provided using optical voltage transducers equipped with GPS signal receivers. The mode-1 voltages at all terminals are calculated using the Clarke's transformation. Discrete wavelet transformation (DWT) is then applied to the calculated mode-1 voltages to obtain the time-frequency components. The squares of wavelet transformation coefficients (WTC²s) of

mode-1 voltages are observed to detect the arrival times at the terminals. The proposed faulty segment identification algorithm and fault location formulation are based on the differences among the first arrival times at all terminals. The effectiveness of the proposed method is evaluated through simulation results of a hybrid seven-terminal transmission system. The transient simulations and the post fault analysis are carried out using EMTP-RV and MATLAB Wavelet Toolbox, respectively. The performance of the proposed algorithm is studied for the following conditions: fault type, grounding system, fault inception angle (FIA), transducer bandwidth, measurement device sampling frequency, fault resistance, non-ideal fault, and non-linear arc. According to the simulation results, the proposed method is able to identify the faulty segment and estimate the fault location. However, its performance reduces in the case of the faults close to the joint point and ending terminals.

APPENDIX A

The ability of the proposed method in detection of faulty segments is discussed in this appendix. The proposed method has no mathematically unidentifiable zones, i.e., the faulty segment can be identified for a fault close to the joint point or terminals, provided there is not any uncertainty in the measurements. In order to justify the above claim, if there is no uncertainty in arrival time detection, ε is removed from (1) and (4). Therefore, the arrival time differences are

$$\begin{cases} \tilde{\tau}_{mn} = (2\lambda - 1)\tau_m - \tau_n, \text{ if } m\text{-}J \text{ is faulty} \\ \tilde{\tau}_{mn} = (1 - 2\lambda)\tau_n + \tau_m, \text{ if } n\text{-}J \text{ is faulty} \\ \tilde{\tau}_{mn} = \tau_m - \tau_n, \text{ neither } m\text{-}J \text{ nor } n\text{-}J \text{ is faulty} \end{cases} \quad (16)$$

Considering (6), the elements of the matrix \mathbf{A} are

$$\begin{aligned} \Delta_{mn} &= |(2\lambda - 1)\tau_m - \tau_n - (\tau_m - \tau_n)|, \text{ if } m\text{-}J \text{ is faulty} \\ \Delta_{mn} &= |(1 - 2\lambda)\tau_n + \tau_m - (\tau_m - \tau_n)|, \text{ if } n\text{-}J \text{ is faulty} \\ \Delta_{mn} &= |\tau_m - \tau_n - (\tau_m - \tau_n)|, \text{ neither } m\text{-}J \text{ nor } n\text{-}J \text{ is faulty} \end{aligned}$$

This can be written as

$$\begin{cases} \Delta_{mn} = 2(\lambda - 1)\tau_m, \text{ if } m\text{-}J \text{ is faulty} \\ \Delta_{mn} = 2(1 - \lambda)\tau_n, \text{ if } n\text{-}J \text{ is faulty} \\ \Delta_{mn} = 0, \text{ neither } m\text{-}J \text{ nor } n\text{-}J \text{ is faulty} \end{cases} \quad (17)$$

It is noticed from (17) that the elements of the matrix \mathbf{A} are a function of the wave traveling time in the faulty segment and the fault location. Then, the index of the column or row with $\Delta_{ij} > 0$ shows the faulty segment, unless $\lambda = 1$. Thus, the proposed method is not affected by the size of the system, the length of the segments, and the fault location.

However, measurement uncertainties slightly change the values of the elements of the matrix \mathbf{A} (as shown in Table I). Therefore, for a fault close to the joint point ($\lambda \rightarrow 1$), the elements of the matrix \mathbf{A} become close to one another, and the proposed method probably fails to identify the faulty segment, and subsequently, the fault location cannot be estimated.

APPENDIX B

Remark: If $X_1 \sim \mathcal{N}(0, \sigma_1^2)$ and $X_2 \sim \mathcal{N}(0, \sigma_2^2)$ are two

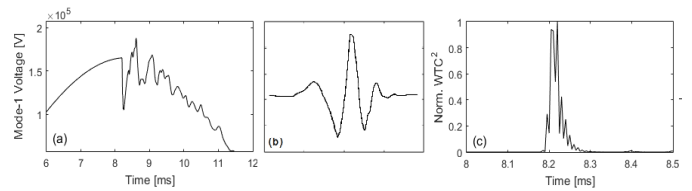


Fig. C1. (a) Typical fault induced distortion in the voltage waveform. (b) db-4 mother wavelet. (c) The resulted normalized WTC².

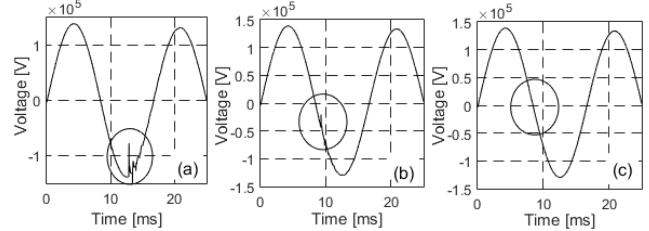


Fig. C2. The relationship between FIA and arriving waves. (a) $FIA \approx 90^\circ$. (b) $FIA \approx 15^\circ$. (c) $FIA \approx 0^\circ$.

independent Gaussian random variables, then $(X_1 - X_2) \sim \mathcal{N}(0, \sigma_1^2 + \sigma_2^2)$. As the uncertainties in the arrival time measurements are related to TR noises, the elements of the diagonal weight matrix (i.e., \mathbf{R}^{-1} in (10)) are selected according to the noise variances of TRs. Thus, $\mathbf{R}_{(N-1) \times (N-1)} = \text{diag}(\sigma_m^2 + \sigma_{c^*}^2), \forall m = 1, 2, \dots, N, m \neq c^*$ and the solution to (10) is

$$\hat{\lambda} = 1/2 (\mathbf{t}^* \mathbf{R}^{-1} \mathbf{t}^*)^{-1} \mathbf{t}^{*T} \mathbf{R}^{-1} \mathbf{b} \quad (18)$$

where the variables are defined in (10). It is noted that this estimator is not robust against outliers. A robust estimator based on least-absolute-value (LAV) may be used instead, as suggested in [19].

APPENDIX C

Daubechies-4 (db-4) mother wavelet is selected for detection of the discontinuities induced by fault initiated waves because of its wide use in fault location literature and according to our investigations of different mother wavelets such as Haar and Symlet. A typical fault induced distortion in the voltage waveform, db-4 mother wavelet, and the resulted normalized WTC² are shown in Figs. C1(a), C1(b), and C1(c), respectively.

Since the sensitivity of the proposed method to FIA is studied, the effect of the FIA on the arriving waves is shown in Fig. C2 (SLG fault in the middle of Segment 1-J, $Z_f = 1 \Omega$, $F_s = 200 \text{ kHz}$). Fig. C2(a) shows the mode-1 voltage for a fault with $FIA \approx 90^\circ$ that generates large arriving waves. Fig. C2(b) shows the mode-1 voltage for a fault with $FIA \approx 15^\circ$ that generates smaller arriving waves compared to the first one. Fig. C2(c) shows the mode-1 voltage for a fault with $FIA \approx 0^\circ$ where no arriving wave is detected.

REFERENCES

- [1] ABB Grid Systems - Offshore Wind Connections. (2003, Nov.). ABB Goes Offshore Products and Solutions for Offshore Wind Energy. ABB, Sweden, [Online]. available: www.abb.com/windpower
- [2] C. F. Jensen, C. L. Bak, and U. S. Gudmundsdottir, "Online travelling wave-based fault location on crossbonded ac cables in underground transmission systems," in *Proc. CIGRE*, Paris, 2014.

- [3] Nexans Deutschland Industries GmbH – Energy Networks. (2008, May). Submarine Power Cables. Nexans, Hannover, Germany, [Online]. available: www.nexans.de
- [4] *IEEE Guide for Fault Location Techniques on Shielded Power Cable Systems*, IEEE Standard 1234, 2007.
- [5] *IEEE Guide for Determining Fault Location on AC Transmission and Distribution Lines*, IEEE Standard C37.114, 2004.
- [6] D. A. Tziouvaras, “Protection of high-voltage ac cables, in power systems,” in *Proc. Advanced Metering, Protection, Control, Communication, and Distributed Resources*, Clemson, SC, Mar. 2006, pp. 316–328.
- [7] C. F. Jensen, “Fault in transmission cables and current fault location methods,” in *Online Location of Faults on AC Cables in Underground Transmission Systems*, Switzerland: Springer, 2014, ch 2, pp. 7-18.
- [8] S. W. Min, J. K. Park, S. R. Nam, S. H. Kang, and W. K. Park, “Fault location algorithm for underground power cables using analytical method,” in *Proc. CIGRE*, Paris, 2006.
- [9] S. W. Min, S. R. Nam, S. H. Kang, and J. K. Park, “Fault location algorithm for cross-bonded cables using the singularity of the sheath impedance matrix,” *Electrical Engineering*, vol. 89, no. 7, pp. 525–533, Jul. 2007.
- [10] X. Yang, M. S. Choi, S. J. Lee, C. W. Ten, and S. I. Lim, “Fault location for underground power cable using distributed parameter approach,” *IEEE Trans. Power Systems*, vol. 23, no. 4, pp. 1809-1816, Nov. 2008.
- [11] Z. Xu and T. S. Sidhu, “Fault location method based on single-end measurements for underground cables,” *IEEE Trans. Power Delivery*, vol. 26, no. 4, pp. 2845-2854, Oct. 2011.
- [12] D. S. Gazzana, G. D. Ferreira, A. S. Bretas, A. L. Bettioli, A. Carniato, L. F. N. Passos, A. H. Ferreira, and J. E. M. Silva, “An integrated technique for fault location and section identification in distribution systems,” *Electric Power System Research*, vol. 115, pp. 65-73, 2014.
- [13] S. L. Zimath, M. A. Ramos, J. S. Filho, J. M. Beck, and N. Mueller, “Traveling wave-based fault location experiences,” in *Proc. Protective Relay Eng.*, College Station, TX, pp. 1-7, Mar.-Apr. 2010.
- [14] L. Coffeen, J. McBride, and D. Cantrelle, “Initial development of EHV bus transient voltage measurement: an addition to on-line transformer FRA,” in *Proc. EPRI Substation Equipment Diagnostics*, Orlando, FL., Mar. 2008.
- [15] A. O. Ibe and B. J. Cory, “A travelling wave-based fault locator for two- and three-terminal networks,” *IEEE Trans. Power Delivery*, vol. 1, no. 2, pp. 283-288, Apr. 1986.
- [16] F. H. Magnago and A. Abur, “Fault location using wavelets,” *IEEE Trans. Power Delivery*, vol. 13, no. 4, pp. 1475-1480, Oct. 1998.
- [17] C. Y. Evrenosoglu and A. Abur, “Travelling wave based fault location for teed circuits,” *IEEE Trans. Power Delivery*, vol. 20, no. 2, pp. 1115-1121, Apr. 2005.
- [18] Z. Yongli and F. Xinqiao, “Fault location scheme for a multi-terminal transmission line based on current traveling waves,” *Electrical Power and Energy Systems*, vol. 53, pp. 367-374, Dec. 2013.
- [19] M. Korkali and A. Abur, “Robust fault location using least-absolute-value estimator,” *IEEE Trans. Power Systems*, vol. 28, no. 4, pp. 4384-4392, Nov. 2013.
- [20] H. Livani and C. Y. Evrenosoglu, “A traveling wave based single-ended fault location algorithm using DWT for overhead lines combined with underground cables,” in *Proc. IEEE PES GM*, Minneapolis, MN., pp.1-6, Jul. 2010.
- [21] H. Livani and C. Y. Evrenosoglu, “A machine learning and wavelet-based fault location method for hybrid transmission lines,” *IEEE Trans. Smart Grid*, vol. 5, no. 1, pp. 51-59, Jan. 2014.
- [22] C. F. Jensen, O. M. K. K. Nanayakkara, A. D. Rajapakse, U. S. Gudmundsdottir, and C. L. Bak, “Online fault location on AC cables in underground transmission systems using sheath currents,” *Electric Power Systems Research*, vol. 115, pp. 74-79, Oct. 2014.
- [23] R. J. Hamidi and H. Livani, “A travelling wave-based fault location method for hybrid three-terminal circuits,” in *Proc. IEEE PES GM*, Denver, CO., pp. 1-5, Jul. 2015.
- [24] EMTP-RV 3, Line Data Example, [Online]. Available: <http://emtp.com/content/download>
- [25] Nexans. (2011, Oct.). 60-500 kV High Voltage Underground Power Cables XLPE Insulated Cables. Nexans, Paris, France, [Online]. available: <http://www.nexans.com>
- [26] R. J. Hamidi, S. H. Hosseinian, S. H. H. Sadeghi, and Z. Qu, “A novel approach to utilize PLC to detect corroded and eroded segments of power transmission lines,” *IEEE Trans. Power Delivery*, vol. 30, no. 2, pp. 746-754, Feb. 2015.
- [27] H. W. Dommel, “Overhead transmission lines,” in *EMTP Theory Book*, USA: BPA, 1995, ch 4, pp. 64-149.
- [28] X. Lin, F. Zhao, G. Wu, Z. Li, and H. Weng, “Universal wavefront positioning correction method on traveling-wave-based fault-location algorithms,” *IEEE Trans. Power Delivery*, vol. 27, no. 3, pp. 1601-1610, Jul. 2012.
- [29] L. U. Iurinic, R. G. Ferraz, A. S. Bretas, A. L. Bettioli, L. F. N. dos Passos, A. Carniato, I. K. Khairalla, R. Z. Homma, and A. Baader, “Fault induced transient detection in power systems: an adaptive approach considering noisy environment,” in *Proc. IPST*, Cavtat, Croatia, Jun. 2015.
- [30] K. R. Caino de Oliveira, R. H. Salim, A. Shuck Jr., and A. S. Bretas, “Faulted branch identification on power distribution systems under noisy environment,” in *Proc. IPST*, Kyoto, Japan, Jun. 2009.
- [31] V. De Andrade and E. Sorrentino, “Typical expected values of the fault resistance in power systems,” in *Proc. T&D-LA*, Sao Paulo, Brazil, pp. 602-609, Nov. 2010.
- [32] *Short-Circuit Currents in Three-Phase A.C. Systems –Part 3: Currents during Two Separate Simultaneous Line-to-Earth Short Circuits and Partial Short-Circuit Currents Flowing through Earth*, IEC 60909-3, Second Edition, Sep. 2003.
- [33] T. Shindo and T. Suzuki, “A new calculation method of breakdown voltage-time characteristics of long air gaps,” *IEEE Trans. Power Apparatus and Systems*, vol. PAS-104, no. 6, pp. 1556-1563, Jun. 1985.
- [34] X. Zhou, S. Chen, H. Wang, R. Zeng, C. Zhuang, J. Yu, and Y. Ding, “Experiment on leader propagation characteristics of air gaps in UHVDC transmission towers under positive switching impulse voltages,” *CSEE Journal of Power and Energy Systems*, vol. 1, no. 3, pp. 42-48, Sep. 2015.
- [35] EMTP-RV 3, Air Gap Leader Example, [Online]. Available: <http://emtp.com/content/download>
- [36] M. Kizilcay and T. Pniok, “Digital simulation of fault arcs in power systems,” *ETEP*, vol. 1, no. 1, pp. 55-60, Jan. 1991.
- [37] M. Majidi, M. Etezadi-Amoli, and M. Sami-Fadali, “A sparse-data-driven approach for fault location in transmission networks,” *IEEE Trans. Smart Grid*, vol. PP, no. 99, pp. 1-9, Nov. 2015.
- [38] J. J. Guo and S. A. Boggs, “High frequency signal propagation in solid dielectric tape shielded power cables,” *IEEE Trans. Power Delivery*, vol. 26, no. 3, pp. 1793–1802, Jul. 2011.
- [39] C. K. Jung, J. B. Lee, X. H. Wang, and Y. H. Song, “Wavelet based noise cancellation technique for fault location on underground power cables,” *Electric Power Systems Research*, vol. 77, no. 10, pp. 1349-1362, Aug. 2007.
- [40] M. Gilany, D. k. Ibrahim, and E. S. Tag Eldin, “Traveling-wave-based fault-location scheme for multiend-aged underground cable system,” *IEEE Trans. Power Delivery*, vol. 22, no. 1, pp. 82-89, Jan. 2007.
- [41] P. Chen and K. Wang, “Fault location technology for high-voltage overhead lines combined with underground power cables based on travelling wave principle,” In *Proc. APAP*, Beijing, China, vol. 1, pp. 784-751, Oct. 2011.